

## Supplemental methods

**Flow cytometry analysis.** The cultured PPCs (passage 3 to passage 5) were prepared for flow cytometry analysis with fluorochrome conjugated antibodies including CD45 monoclonal antibody (1:200; ThermoFisher, #64-9459-42), CD90.2 monoclonal antibody (1:200; ThermoFisher, #47-0902-82), and Sca1 monoclonal antibody (1:150; ThermoFisher, #45-5981-82).

**ChIP assay.** PPCs (passage 3 to passage 5,  $2 \times 10^6$ ) were harvested and fixed with formaldehyde. Chromatin was fragmented by sonication to shear DNA to 200-500 bp in size. Chromatin fragments were immunoprecipitated using Dnmt3b antibody (1:50; Abcam, #ab2851). Histone H3 (1:50; Cell Signaling, #4620) and IgG (1:50; Cell Signaling, #2729) antibodies were used as positive and negative controls, respectively. After reverse crosslinking, the enrichment of *Rbpjk* DNA fragment was assessed by real-time qPCR. Primer sequences used for CpG islands in *Rbpjk* were forward, 5'-CTAGGTGACTCAGATGCATGAC-3', and reverse, 5'-TCCCGAGCCTGGTACTT-3'; primer sequences for CpG Island 2 in *Rbpjk* gene body were forward, 5'-CCTTTGTTTCGCCGCTTA-3', and reverse, 5'-CCAGCTACTGAAGAGAGGGATA-3'.

**Fabrication of cell impregnated tissue constructs.** A simultaneous electrospinning and electro spraying approach was used to fabricate cell impregnated tissue constructs. The electro spraying stream contained suspension of adipose derived GFP+ progenitor cells (Cyagen, #MUBMD-01101) or dCas9-Dnmt3a-Rbpjk gRNA modified  $C_3H_{10}T_{1/2}$  cells with a density of  $4 \times 10^6$  cells/ml. The electrospinning stream was 10% polycaprolactone (PCL; Millipore Sigma, #440744) solution in chloroform. The electro spraying and electrospinning streams were loaded into syringe pumps. The needles of the two streams were charged at +18 kV and +24 kV, respectively. The injection rates of the PCL solution and cell suspension was controlled at 5 ml/h and 1.2 ml/h, respectively. The rotating collection mandrel was charged at -10 kV. The fabrication was conducted under an environment with 30% humidity. After fabricating for 30 minutes, the tissue construct was immersed in culture medium to remove residual solvent. The medium was changed twice. To observe live cells in the fabricated tissue constructs, confocal images were taken using a confocal microscope. Z-stack images were reconstructed. The morphology of tissue constructs was evaluated by SEM. To determine live cell density in the tissue constructs, the samples were incubated with papain solution followed by quantifying dsDNA content using Quant-iT dsDNA assay kit (ThermoFisher, #Q33233). The cell density was calculated based on calibration curve.

## Supplemental figures

**Figure S1. A schematic depicts experimental design for single cell RNA sequencing of fracture callus.**

**Figure S2. Systemic inflammation alters cellular distribution in fracture callus. (A)** t-distributed stochastic embedding (tSNE) visualization of cell clustering in control and RA fracture callus. Annotated post hoc and colored by clustering. **(B)** Bar plots of inflammatory related cell counts in control and RA fracture callus.

**Figure S3. Systemic inflammation alters genetic profiling of cells in fracture callus.** Dot plots to visualize the changes of key feature expression across cell clusters. The size scale of the dots represents the percentage of cells within a cluster, while the color scale encodes the average expression level across all cells within a cluster. Key cell-type maker genes were plotted for **(A)** myeloid, **(B)** mesenchymal, and **(C)** endothelial lineage respectively. **(D)** Dot plots of key transcriptional factors of Notch, Wnt, TGFb, and Hedgehog signaling across cluster 13 and cluster 1 in control and RA fracture callus at 7 dpf.

**Figure S4. RA, aging and obesity induces elevated inflammation in fracture callus.** Real-time qPCR analyses of gene expression for *Il1b* and *Tnfa* in 5 dpf fracture callus isolated from (A) RA mice, (B) 18-month-old mice and (C) high-fat-diet induced obese mice (n=4). Data presented as mean  $\pm$  SD. \* $p < 0.05$  by Student's t test.

**Figure S5. IL1b treatment induces intrinsic inflammatory responses in primary PPCs.** (A) Flow cytometry analysis of surface makers' expression in primary PPCs, including CD45, CD90 and Sca1. (B) Real-time qPCR analyses of gene expression for *Ikk2*, *Il1b*, *Il6*, and *Tnfa* in vehicle and IL1b treated primary PPCs isolated from 3-month-old wild type mice (n=3). Data presented as mean  $\pm$  SD. \* $p < 0.05$  by Student's t test.

**Figure S6. Cells in fracture callus are derived from Prx1-expressing cells.** (A) Representative fluorescent images for tdTomato (Ai9) on callus sections from *Ai9<sup>f/+</sup>* and *Prx1Cre<sup>ERT2</sup>;Ai9<sup>f/+</sup>* mice at 10 dpf. White dotted line outlined fracture callus. Scale bar, 100  $\mu$ m. (B) Real-time qPCR analyses of gene expression for *Ikk2*, *Il1b* and *Tnfa* in 5 dpf callus tissue from *Ikk2ca<sup>f/+</sup>* (control) and *Prx1Cre<sup>ERT2</sup>;Ikk2ca<sup>f/+</sup>* (*Ikk2ca<sup>Prx1</sup>*) mice (n=5). Data presented as mean  $\pm$  SD. \* $p < 0.05$  by Student's t test.

**Figure S7. *Ikk2ca* in progenitor cells leads to reduced callus remodeling.** (A) TRAP staining of 14 dpf fracture callus sections from *Ikk2ca<sup>f/+</sup>* (control) and *Prx1Cre<sup>ERT2</sup>;Ikk2ca<sup>f/+</sup>* (*Ikk2ca<sup>Prx1</sup>*) mice (n=5). Scale bar, 100  $\mu$ m. (B) Oc.S/BS measured on TRAP staining of *Ikk2ca<sup>f/+</sup>* (control) and *Prx1Cre<sup>ERT2</sup>;Ikk2ca<sup>f/+</sup>* (*Ikk2ca<sup>Prx1</sup>*) fractures (n=5). Data presented as mean  $\pm$  SD. \* $p < 0.05$  by Student's t test.

**Figure S8. Histological assessments determine the effect of *Rbpjk* LOF on fracture repair defects induced by *Ikk2ca*.** Histomorphometry analyses of mesenchyme, cartilage, and bone areas on callus sections from *Ikk2ca<sup>f/+</sup>* (control), *Prx1Cre<sup>ERT2</sup>;Ikk2ca<sup>f/+</sup>* (*Ikk2ca<sup>Prx1</sup>*), *Prx1Cre<sup>ERT2</sup>;Rbpjk<sup>ff</sup>* (*Rbpjk<sup>Prx1</sup>*), and *Prx1Cre<sup>ERT2</sup>;Ikk2ca<sup>f/+</sup>;Rbpjk<sup>ff</sup>* (*Ikk2ca;Rbpjk<sup>Prx1</sup>*) mice at 7, 10, and 14 dpf (n=5). Data presented as mean  $\pm$  SD. \* $p < 0.05$  by two-way ANOVA followed by Tukey test.

**Figure S9. MicroCT assessments determine the effect of *Rbpjk* LOF on fracture repair defects induced by *Ikk2ca*.** Quantifications of bony callus volume and BV/TV on reconstructed microCT images of *Ikk2ca<sup>f/+</sup>* (control), *Prx1Cre<sup>ERT2</sup>;Ikk2ca<sup>f/+</sup>* (*Ikk2ca<sup>Prx1</sup>*), *Prx1Cre<sup>ERT2</sup>;Rbpjk<sup>ff</sup>* (*Rbpjk<sup>Prx1</sup>*), and *Prx1Cre<sup>ERT2</sup>;Ikk2ca<sup>f/+</sup>;Rbpjk<sup>ff</sup>* (*Ikk2ca;Rbpjk<sup>Prx1</sup>*) fractures at 14 dpf (n=5). Data presented as mean  $\pm$  SD. \* $p < 0.05$  by two-way ANOVA followed by Tukey test.

**Figure S10. TRAP staining assessments determine the effect of *Rbpjk* LOF on fracture repair defects induced by *Ikk2ca*.** (A) TRAP staining of 14 dpf fracture callus sections from *Ikk2ca<sup>f/+</sup>* (control), *Prx1Cre<sup>ERT2</sup>;Ikk2ca<sup>f/+</sup>* (*Ikk2ca<sup>Prx1</sup>*), *Prx1Cre<sup>ERT2</sup>;Rbpjk<sup>ff</sup>* (*Rbpjk<sup>Prx1</sup>*), and *Prx1Cre<sup>ERT2</sup>;Ikk2ca<sup>f/+</sup>;Rbpjk<sup>ff</sup>* (*Ikk2ca;Rbpjk<sup>Prx1</sup>*) mice (n=5). Scale bar, 100  $\mu$ m. (B) Oc.S/BS measured on TRAP staining of *Ikk2ca<sup>f/+</sup>* (control), *Prx1Cre<sup>ERT2</sup>;Ikk2ca<sup>f/+</sup>* (*Ikk2ca<sup>Prx1</sup>*), *Prx1Cre<sup>ERT2</sup>;Rbpjk<sup>ff</sup>* (*Rbpjk<sup>Prx1</sup>*), and *Prx1Cre<sup>ERT2</sup>;Ikk2ca<sup>f/+</sup>;Rbpjk<sup>ff</sup>* (*Ikk2ca;Rbpjk<sup>Prx1</sup>*) fractures (n=5). Data presented as mean  $\pm$  SD. \* $p < 0.05$  by two-way ANOVA followed by Tukey test.

**Figure S11. *Dnmt3b* expression is reduced in *Ikk2ca*-induced inflammatory callus.** Real-time qPCR analyses of gene expression for *Dnmt1*, *Dnmt3a*, and *Dnmt3b* in 5 dpf callus tissue from *Ikk2ca<sup>f/+</sup>* (control) and *Prx1Cre<sup>ERT2</sup>;Ikk2ca<sup>f/+</sup>* (*Ikk2ca<sup>Prx1</sup>*) mice (n=5). Data presented as mean  $\pm$  SD. \* $p < 0.05$  by Student's t test.

**Figure S12. *Dnmt3b* is reduced in PPCs by inflammatory stimuli.** Real-time qPCR analyses of gene expression for *Dnmt1*, *Dnmt3a*, and *Dnmt3b* in vehicle and IL1b treated primary wild type PPCs (n=3). Data presented as mean  $\pm$  SD. \* $p < 0.05$  by Student's t test.

**Figure S13. Rbpjk is a target of Dnmt3b.** (A) Schematic illustration of the two Dnmt3b binding sites (CpG islands in green boxes) identified in *Rbpjk* gene. (B) Pull-down assay of genomic DNA with a Dnmt3b antibody (ChIP) showed interaction of Dnmt3b with its binding sites in *Rbpjk* gene by qPCR (n=3). Data presented as mean  $\pm$  SD. \* $p < 0.05$  by two-way ANOVA followed by Tukey test.

**Figure S14. DNA methylation reduction in Rbpjk gene leads to increased protein expression.** (A) Schematic illustration of the two Dnmt3b binding sites (CpG islands in green boxes) identified in *Rbpjk* gene. Twelve gRNAs were designed to target CpG island 1 (1.5 kb) and CpG island 2 (300 bp). (B) Schematic representing the selection of C<sub>3</sub>H<sub>10</sub>T<sub>1/2</sub> cell lines modified by dCas9-Tet1 epigenetic editing system specifically targeting CpG islands of *Rbpjk* gene. (C) Western blot analyses for Rbpjk in protein extracts from dCas9-Tet1-scramble gRNA (control) and 12 individual dCas9-Tet1-Rbpjk gRNAs engineered C<sub>3</sub>H<sub>10</sub>T<sub>1/2</sub> cell lines (n=3). C, dCas9-Tet1-scramble gRNA. 1-10, dCas9-Tet1-Rbpjk<sub>1-1-10</sub> gRNAs targeting CpG island 1 of *Rbpjk* gene. 11-12, dCas9-Tet1-Rbpjk<sub>2-1-2</sub> gRNAs targeting CpG island 2 of *Rbpjk* gene.

**Figure S15. Gene expression of progenitor differentiation markers to determine the effect of Rbpjk inhibition using an epigenetic modification approach on progenitor differentiation potential.** Real-time qPCR analyses for *Rbpjk*, *Hey1*, *Sox9*, *Col2a1*, *Acan*, *Sp7*, *Rux2*, and *Alp* in dCas9-Dnmt3a-scramble (control) and dCas9-Dnmt3a-Rbpjk<sub>1-9</sub> C<sub>3</sub>H<sub>10</sub>T<sub>1/2</sub> (*Rbpjk* epigenetically modified) cell lines in the presence or absence of IL1b. Data presented as mean  $\pm$  SD. \* $p < 0.05$  by two-way ANOVA followed by Tukey test.

**Figure S16. Tamoxifen and Doxycycline induces Ikk2 and Dnmt3b gene expression in fracture callus.** Real-time qPCR analyses for *Ikk2* and *Dnmt3b* in 5 dpf callus from *Ikk2ca*<sup>f/+</sup> (control) and *Prx1Cre*<sup>ERT2</sup>;*Ikk2ca*<sup>f/+</sup>;*Rosa-rtTA*<sup>f/+</sup>;*Dnmt3b-tg* (*Ikk2ca*;*Dnmt3b-tg*<sup>Prx1</sup>) mice (n=5). Data presented as mean  $\pm$  SD. \* $p < 0.05$  by Student's t test.

**Figure S17. Histological analyses determine the effect of Dnmt3b GOF on fracture repair defects induced by Ikk2ca.** Histomorphometry quantifications of mesenchyme and cartilage areas on callus sections from *Ikk2ca*<sup>f/+</sup> (control), *Prx1Cre*<sup>ERT2</sup>;*Ikk2ca*<sup>f/+</sup> (*Ikk2ca*<sup>Prx1</sup>), *Prx1Cre*<sup>ERT2</sup>;*Rosa-rtTA*<sup>f/+</sup>;*Dnmt3b-tg* (*Dnmt3b-tg*<sup>Prx1</sup>), and *Prx1Cre*<sup>ERT2</sup>;*Ikk2ca*<sup>f/+</sup>;*Rosa-rtTA*<sup>f/+</sup>;*Dnmt3b-tg* (*Ikk2ca*;*Dnmt3b-tg*<sup>Prx1</sup>) mice at 7 and 10dpf, respectively (n=5). Data presented as mean  $\pm$  SD. \* $p < 0.05$  by two-way ANOVA followed by Tukey test.

**Figure S18. MicroCT analyses determine the effect of Dnmt3b GOF on fracture repair defects induced by Ikk2ca.** (A) MicroCT images of mineralized bony calluses from *Ikk2ca*<sup>f/+</sup> (control), *Prx1Cre*<sup>ERT2</sup>;*Ikk2ca*<sup>f/+</sup> (*Ikk2ca*<sup>Prx1</sup>), *Prx1Cre*<sup>ERT2</sup>;*Rosa-rtTA*<sup>f/+</sup>;*Dnmt3b-tg* (*Dnmt3b-tg*<sup>Prx1</sup>), and *Prx1Cre*<sup>ERT2</sup>;*Ikk2ca*<sup>f/+</sup>;*Rosa-rtTA*<sup>f/+</sup>;*Dnmt3b-tg* (*Ikk2ca*;*Dnmt3b-tg*<sup>Prx1</sup>) fractures at 14 dpf (n=5). Scale bar, 0.5 mm. (B) Quantifications of bony callus volume and BV/TV on reconstructed microCT images of *Ikk2ca*<sup>f/+</sup> (control), *Prx1Cre*<sup>ERT2</sup>;*Ikk2ca*<sup>f/+</sup> (*Ikk2ca*<sup>Prx1</sup>), *Prx1Cre*<sup>ERT2</sup>;*Rosa-rtTA*<sup>f/+</sup>;*Dnmt3b-tg* (*Dnmt3b-tg*<sup>Prx1</sup>), and *Prx1Cre*<sup>ERT2</sup>;*Ikk2ca*<sup>f/+</sup>;*Rosa-rtTA*<sup>f/+</sup>;*Dnmt3b-tg* (*Ikk2ca*;*Dnmt3b-tg*<sup>Prx1</sup>) fractures at 14 dpf (n=5). Data presented as mean  $\pm$  SD. \* $p < 0.05$  by two-way ANOVA followed by Tukey test.

**Figure S19. Rbpjk inhibition restores Dnmt3b deficiency mediated PPC differentiation defects.** Chondrogenic pellet and osteogenic differentiation assays were performed within *Dnmt3b*<sup>ff</sup> PPCs following Ad-GFP (control) or Ad-Cre (*Dnmt3b* LOF) transfection in the presence or absence of *Rbpjk* LOF. Alcian blue and alizarin red staining of chondrogenic pellet sections and osteogenic cultures at day 28 and day 21, respectively (n=3).

**Figure S20. Histological analyses determine the effect of Rbpjk LOF on fracture repair defects induced by Dnmt3b LOF.** Histomorphometry quantifications of mesenchyme and cartilage areas on callus sections from *Dnmt3b*<sup>ff</sup> (control), *Prx1Cre*<sup>ERT2</sup>;*Dnmt3b*<sup>ff</sup> (*Dnmt3b*<sup>Prx1</sup>),

*Prx1Cre<sup>ERT2</sup>;Rbpjk<sup>ff</sup> (Rbpjk<sup>Prx1</sup>)*, and *Prx1Cre<sup>ERT2</sup>; Dnmt3b<sup>ff</sup>;Rbpjk<sup>ff</sup> (Dnmt3b;Rbpjk<sup>Prx1</sup>)* mice at 7 and 10dpf, respectively (n=5). Data presented as mean  $\pm$  SD. \* $p < 0.05$  by two-way ANOVA followed by Tukey test.

**Figure S21. MicroCT analyses determine the effect of *Rbpjk* LOF on fracture repair defects induced by *Dnmt3b* LOF.** (A) MicroCT images of mineralized bony calluses from *Dnmt3b<sup>ff</sup>* (control), *Prx1Cre<sup>ERT2</sup>;Dnmt3b<sup>ff</sup> (Dnmt3b<sup>Prx1</sup>)*, *Prx1Cre<sup>ERT2</sup>;Rbpjk<sup>ff</sup> (Rbpjk<sup>Prx1</sup>)*, and *Prx1Cre<sup>ERT2</sup>; Dnmt3b<sup>ff</sup>;Rbpjk<sup>ff</sup> (Dnmt3b;Rbpjk<sup>Prx1</sup>)* fractures at 14 dpf (n=5). Scale bar, 0.5 mm. (B) Quantifications of bony callus volume and BV/TV on reconstructed microCT images of *Dnmt3b<sup>ff</sup>* (control), *Prx1Cre<sup>ERT2</sup>;Dnmt3b<sup>ff</sup> (Dnmt3b<sup>Prx1</sup>)*, *Prx1Cre<sup>ERT2</sup>;Rbpjk<sup>ff</sup> (Rbpjk<sup>Prx1</sup>)*, and *Prx1Cre<sup>ERT2</sup>; Dnmt3b<sup>ff</sup>;Rbpjk<sup>ff</sup> (Dnmt3b;Rbpjk<sup>Prx1</sup>)* fractures at 14 dpf (n=5). Data presented as mean  $\pm$  SD. \* $p < 0.05$  by two-way ANOVA followed by Tukey test.

**Figure S22. TRAP staining assessments determine the effect of *Rbpjk* LOF on RA fracture repair.** (A) TRAP staining of 14 dpf fracture callus sections from *Rbpjk<sup>ff</sup>* (control) and *Prx1Cre<sup>ERT2</sup>;Rbpjk<sup>ff</sup> (Rbpjk<sup>Prx1</sup>)* RA mice (n=5). Scale bar, 100  $\mu$ m. (B) Oc.S/BS measured on TRAP staining of *Rbpjk<sup>ff</sup>* (control) and *Prx1Cre<sup>ERT2</sup>;Rbpjk<sup>ff</sup> (Rbpjk<sup>Prx1</sup>)* RA fractures (n=5). Data presented as mean  $\pm$  SD. \* $p < 0.05$  by Student's t test.

**Figure S23. Progenitors fabricated in PCL scaffolds are capable of differentiating and forming calluses at fracture site.** (A) Schematic illustration of the simultaneous electrospinning and electro spraying system for cell impregnated tissue construct fabrication. (B) Representative SEM images of the PCL scaffold with adipose derived GFP+ progenitor cells (n=3). (C) Representative confocal images of PCL scaffolds with adipose derived GFP+ progenitor cells (n=3). (D) Fluorescent images of frozen callus sections of 10-dpf wild type fractures grafted with PCL scaffolds that were fabricated with adipose derived GFP+ progenitor cells. White dotted line outlined cortical bones. Scale bar, 100  $\mu$ m.

**Figure S24. Angiogenesis is restored by epigenetically modified cells on RA fracture callus.** Immunofluorescent staining for endomucin in 14 dpf callus sections from wild type RA fractures grafted with PCL scaffolds that were fabricated with dCas9-Dnmt3a-scramble (control) or dCas9-Dnmt3a-Rbpjk<sup>1-9</sup> C<sub>3</sub>H<sub>10</sub>T<sub>1/2</sub> cells (*Rbpjk* epigenetically modified) (n=5). Scale bar, 100  $\mu$ m.

**Figure S25. TRAP staining assessments to determine the effect of epigenetically modified cells on RA fracture repair.** (A) TRAP staining of callus sections from 14 dpf wild type RA fractures grafted with PCL scaffolds that were fabricated with dCas9-Dnmt3a-scramble (control) or dCas9-Dnmt3a-Rbpjk<sup>1-9</sup> C<sub>3</sub>H<sub>10</sub>T<sub>1/2</sub> cells (*Rbpjk* epigenetically modified) (n=5). Scale bar, 100  $\mu$ m. (B) Oc.S/BS measured on TRAP staining of RA fractures grafted with PCL scaffolds that were fabricated with dCas9-Dnmt3a-scramble (control) or dCas9-Dnmt3a-Rbpjk<sup>1-9</sup> C<sub>3</sub>H<sub>10</sub>T<sub>1/2</sub> cells (*Rbpjk* epigenetically modified) (n=5). Data presented as mean  $\pm$  SD. \* $p < 0.05$  by Student's t test.

Fig. S1

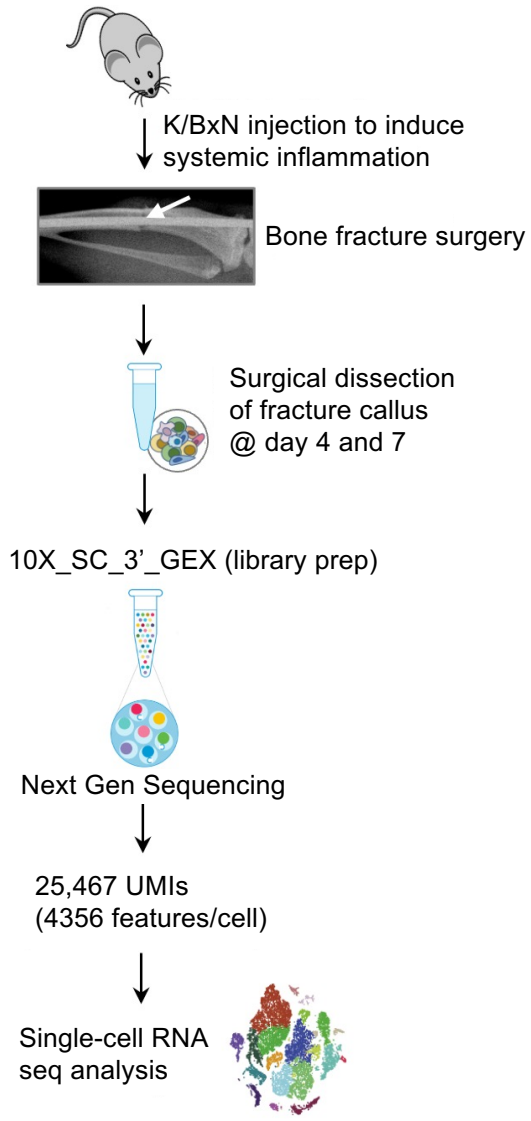


Fig. S2

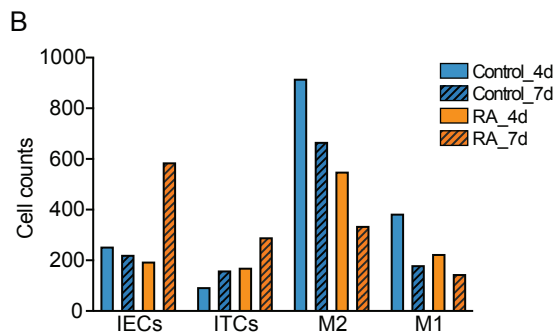
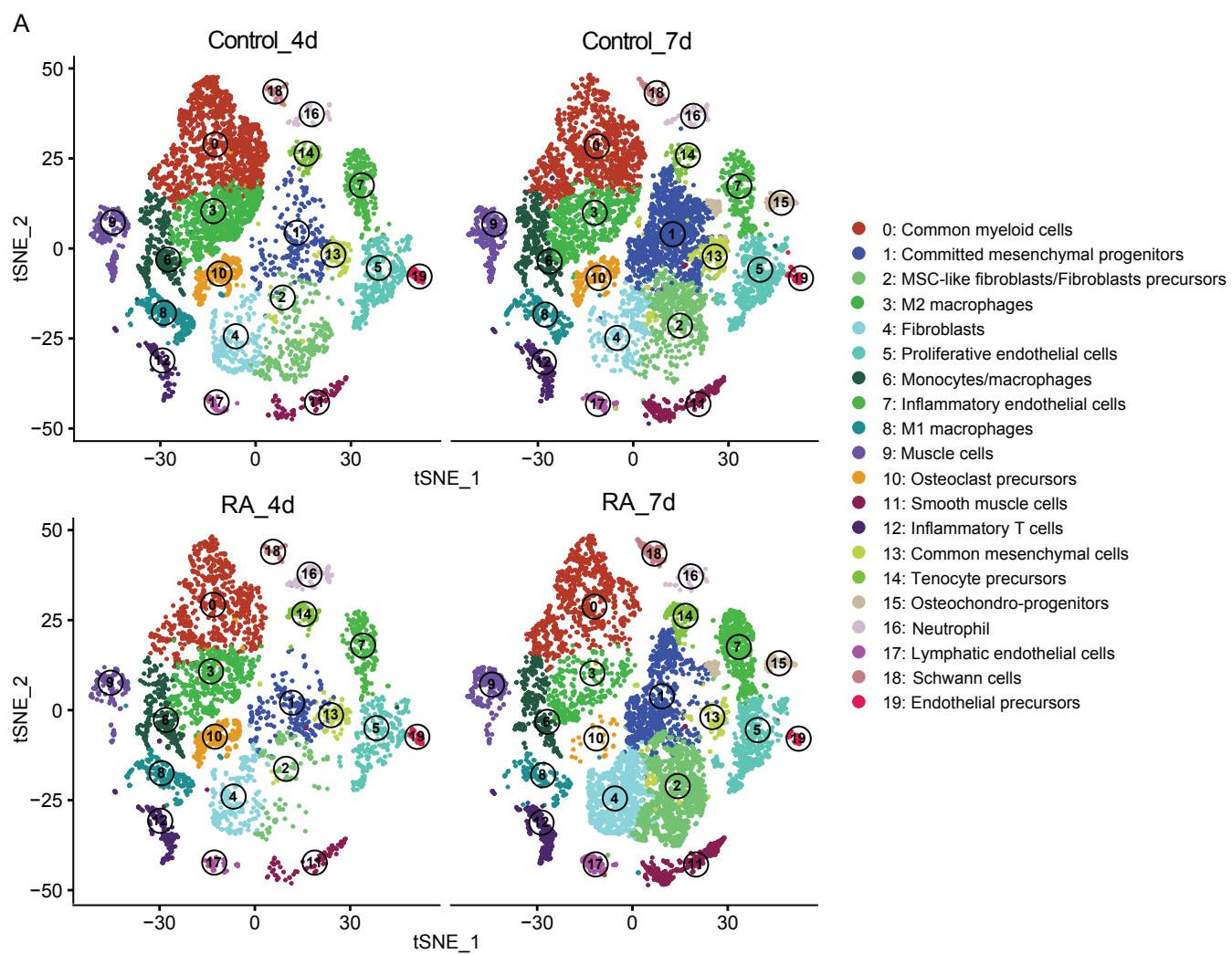


Fig. S3

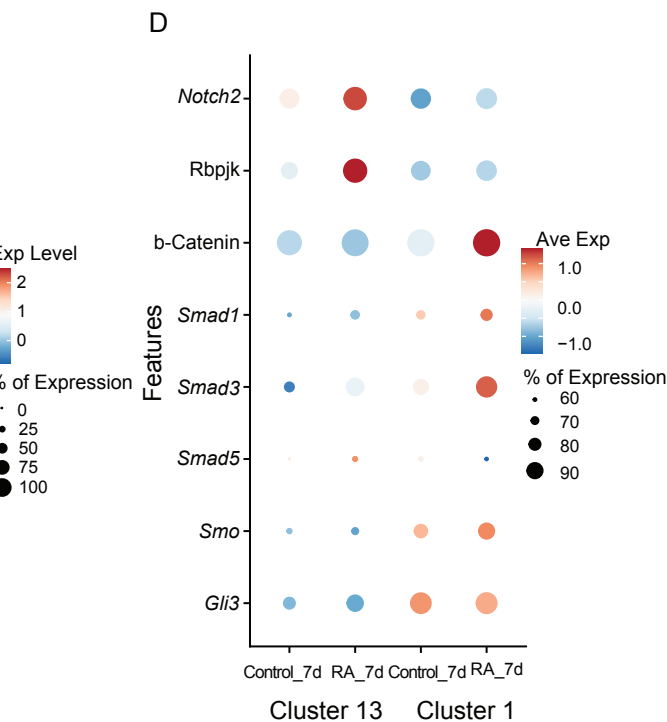
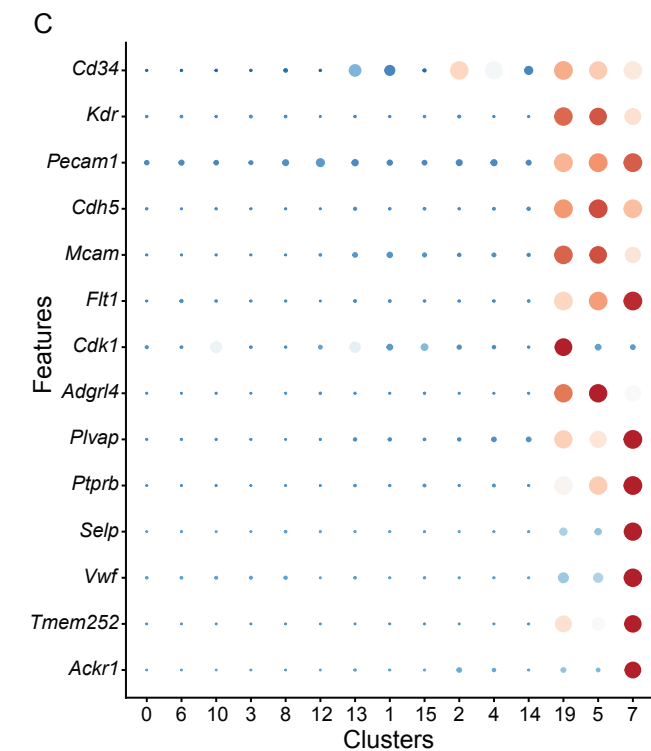
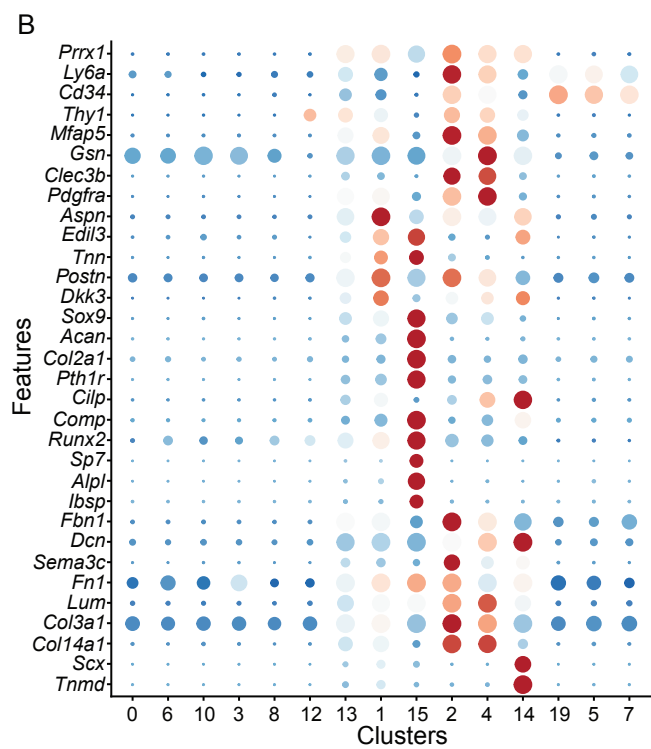
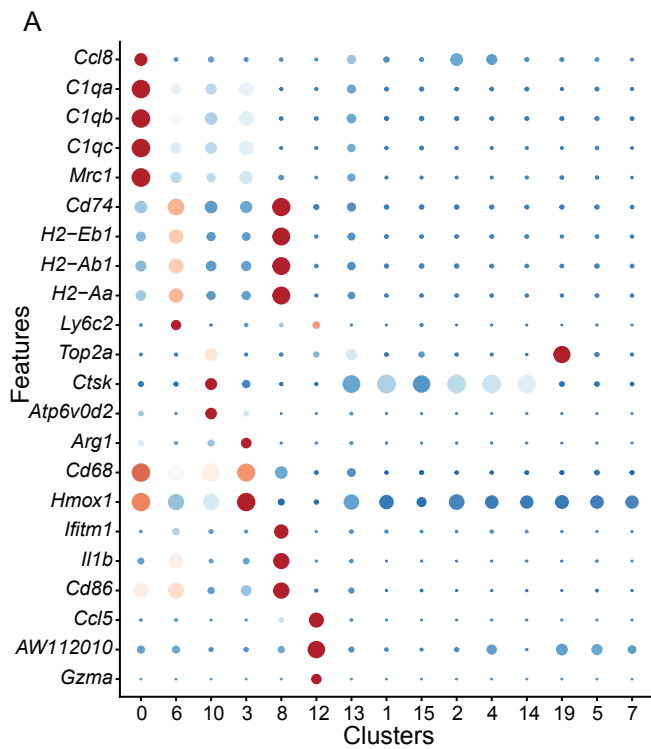


Fig. S4

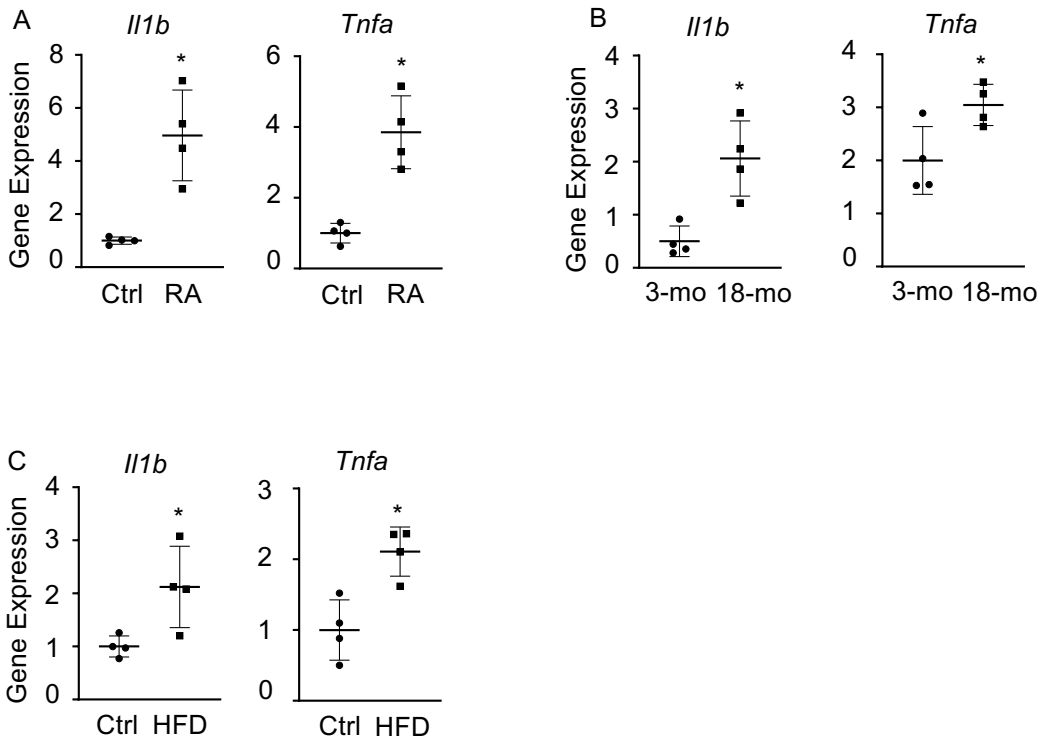


Fig. S5

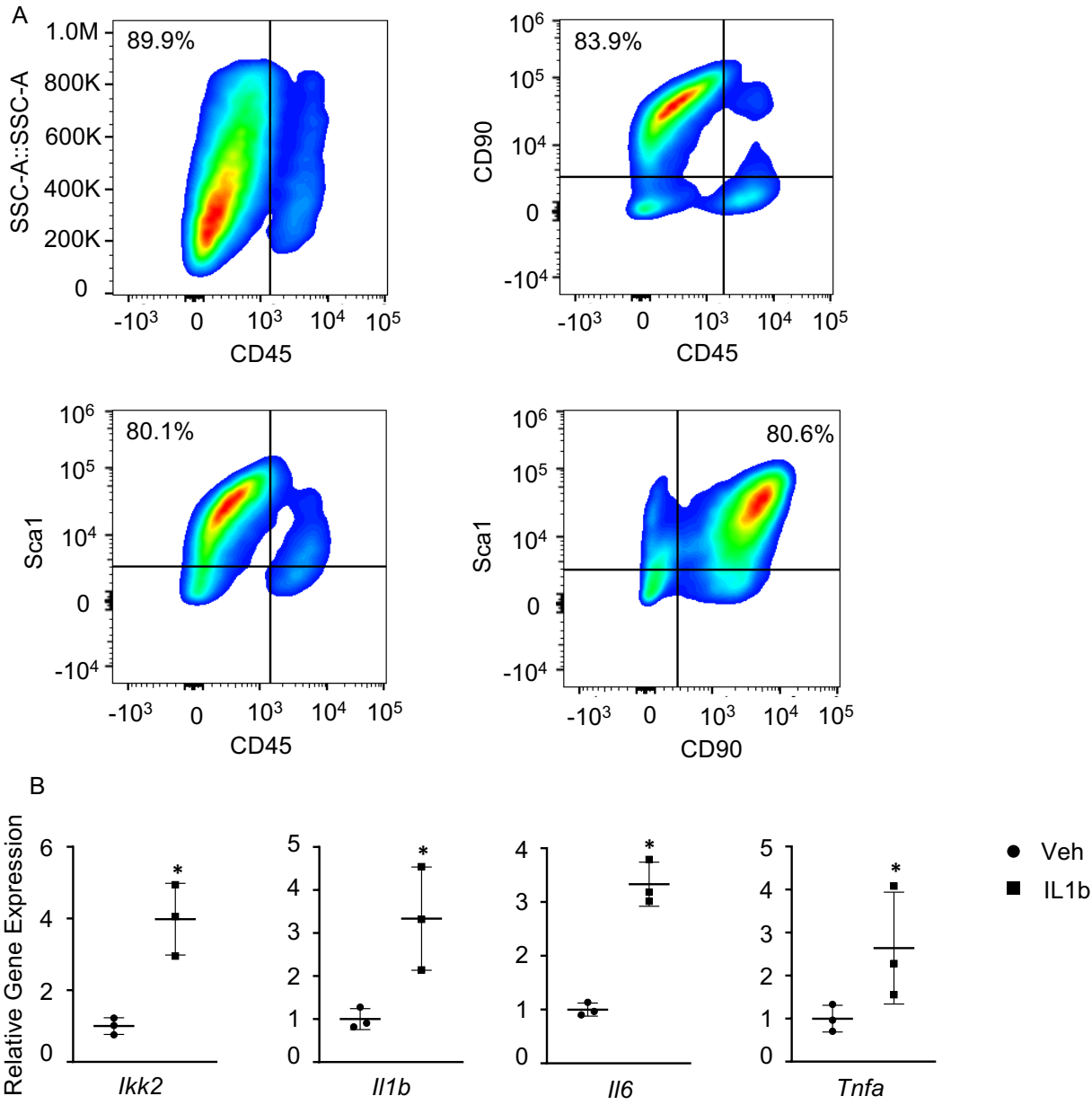


Fig. S6

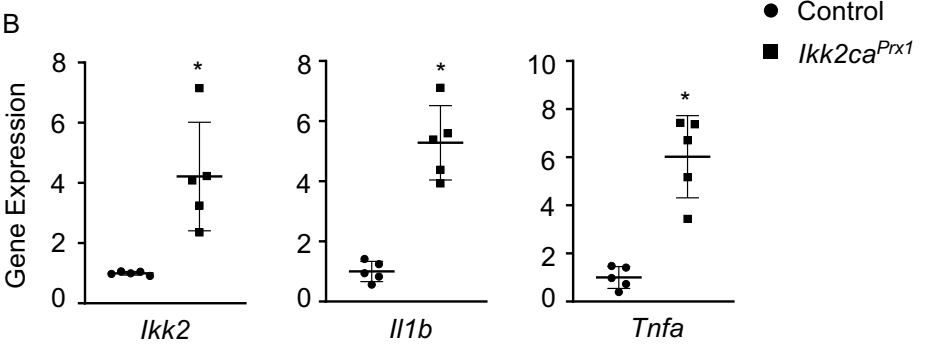
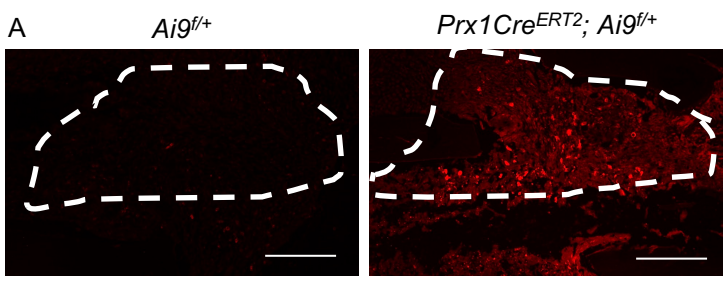


Fig. S7

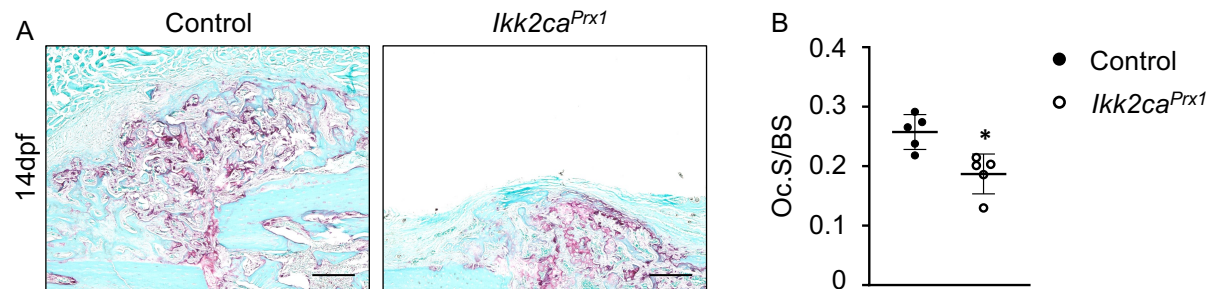


Fig. S8

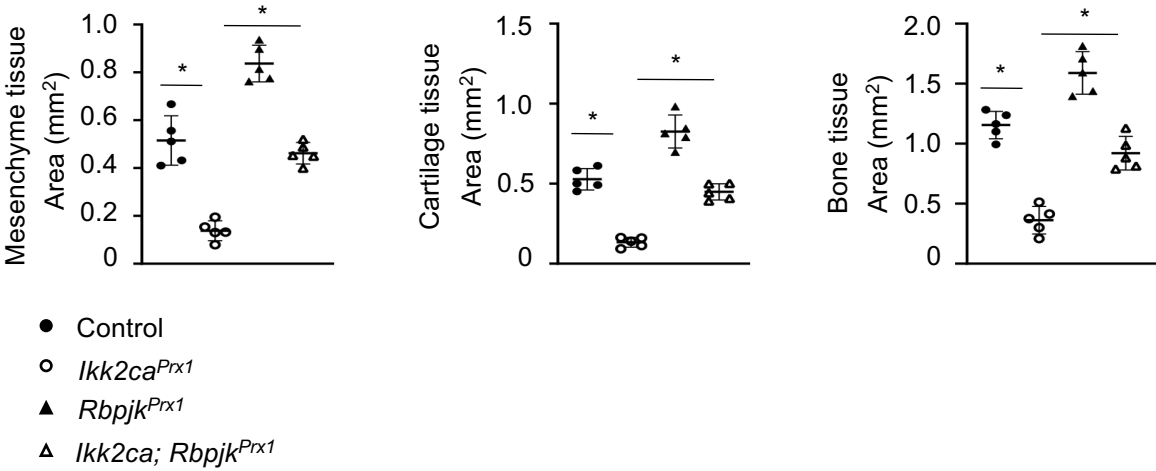


Fig. S9

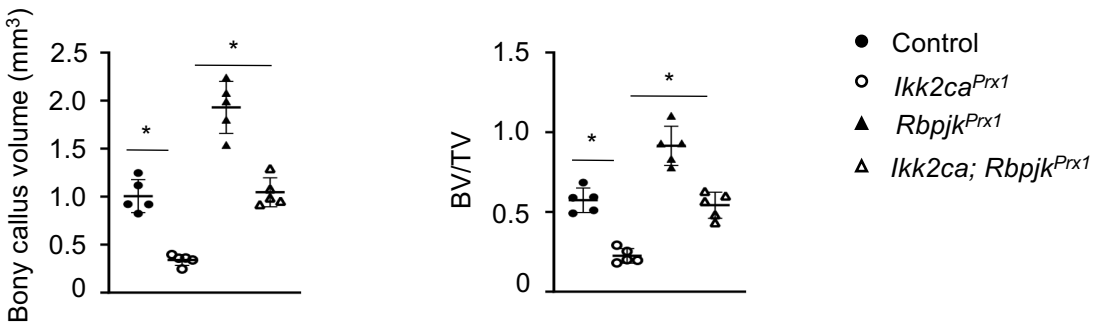


Fig. S10

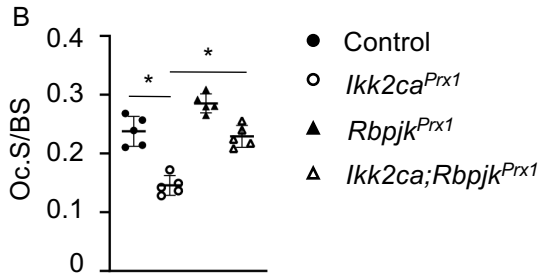
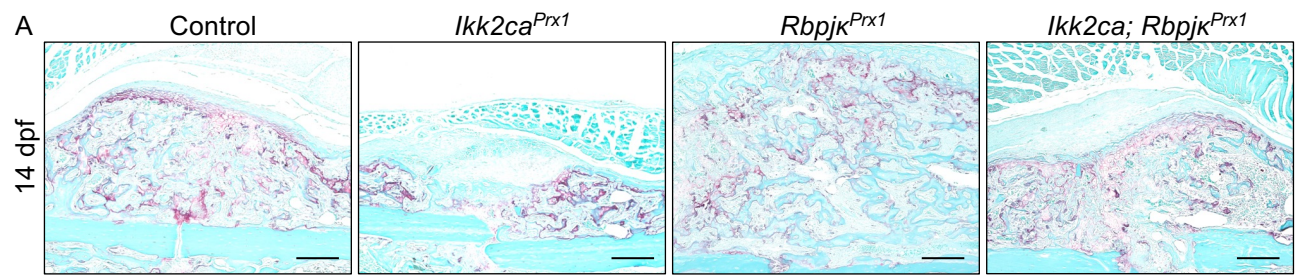


Fig. S11

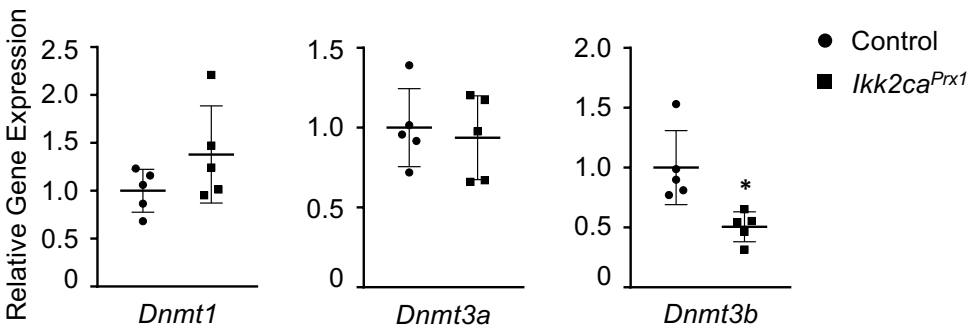


Fig. S12

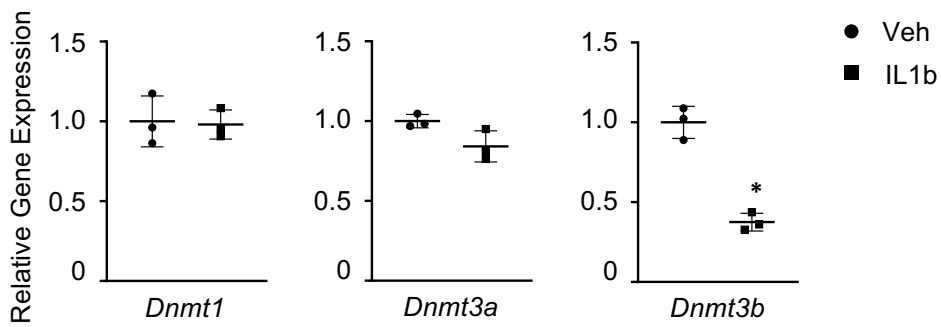


Fig. S13

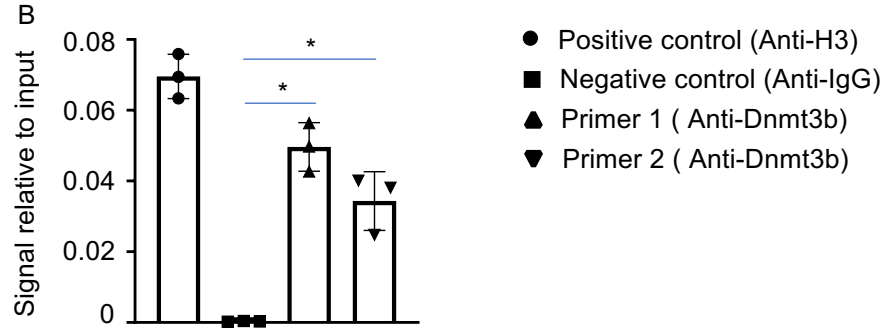
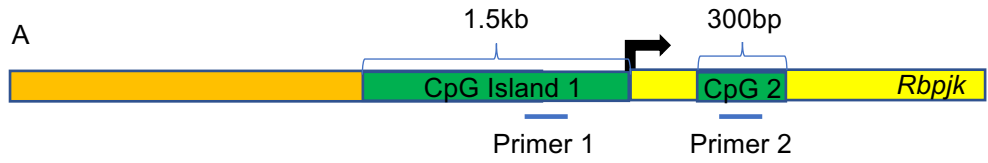


Fig. S14

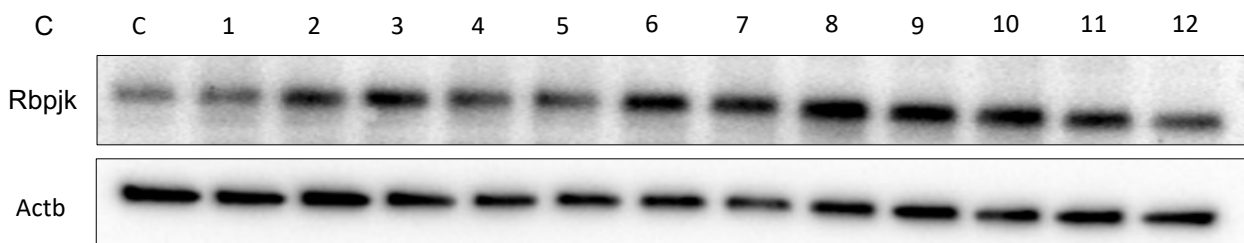
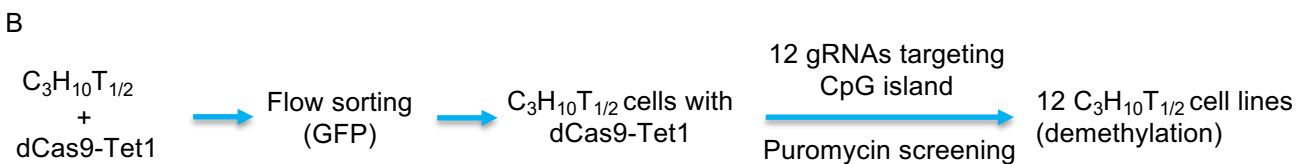
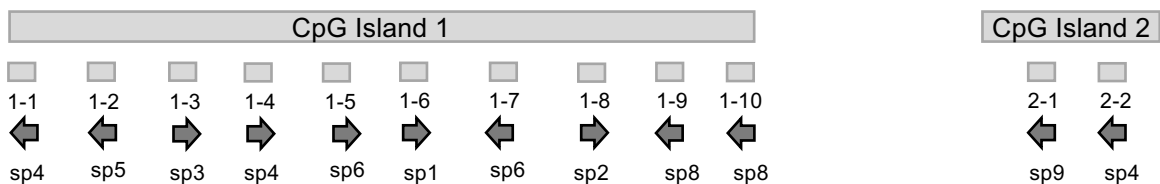
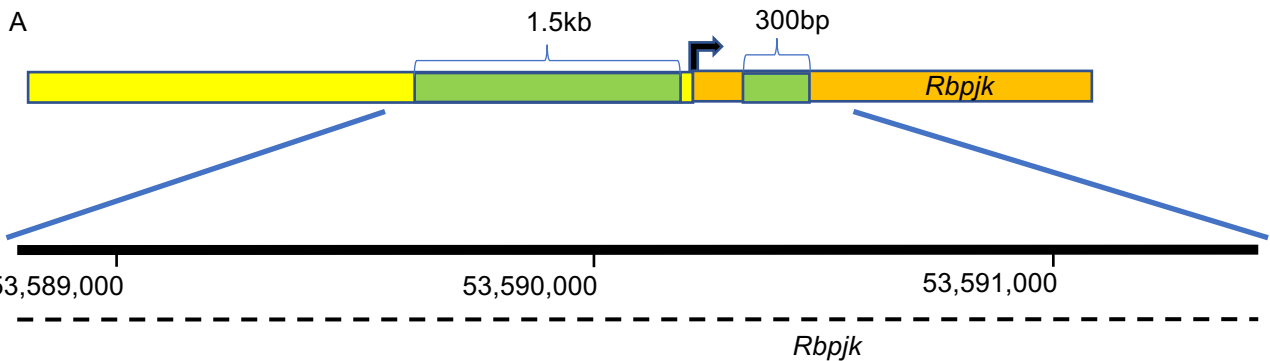
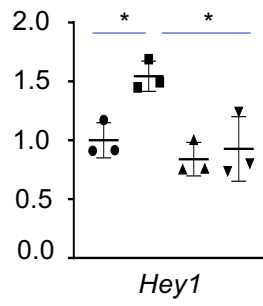
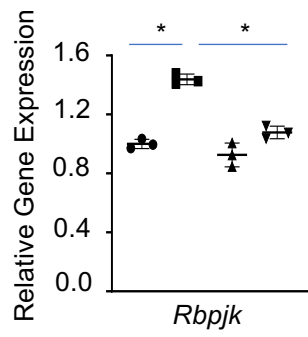


Fig. S15



dCas9-Dnmt3a-scramble cells

- Veh
- IL1b

dCas9-Dnmt3a-Rbpjk<sub>1-9</sub> cells

- ▲ Veh
- ▼ IL1b

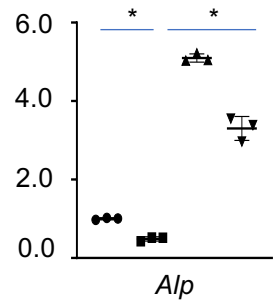
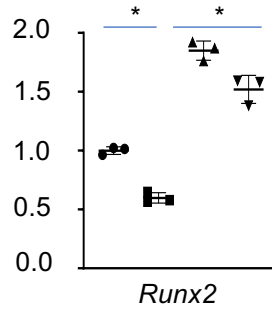
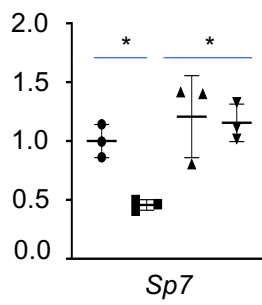
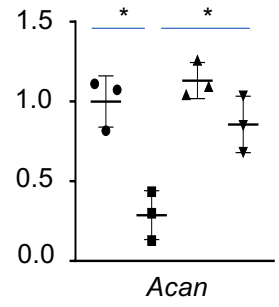
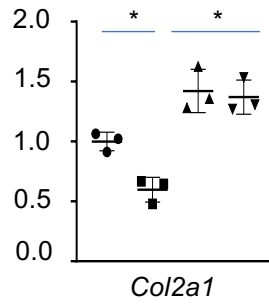
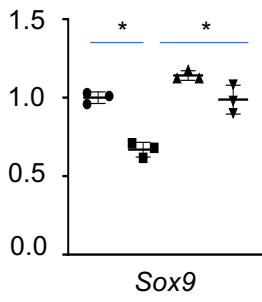


Fig. S16

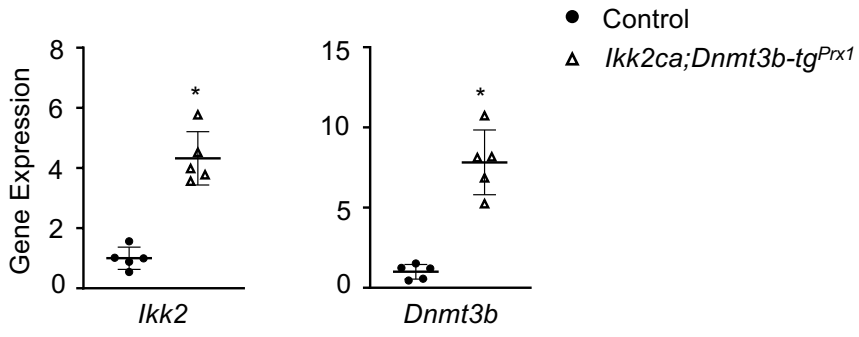


Fig. S17

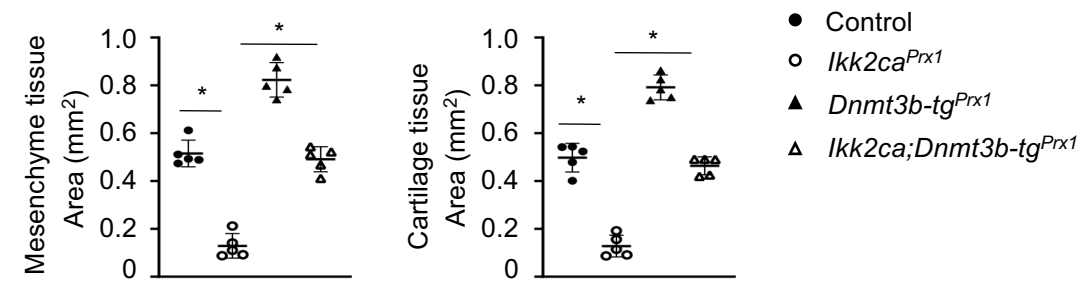


Fig. S18

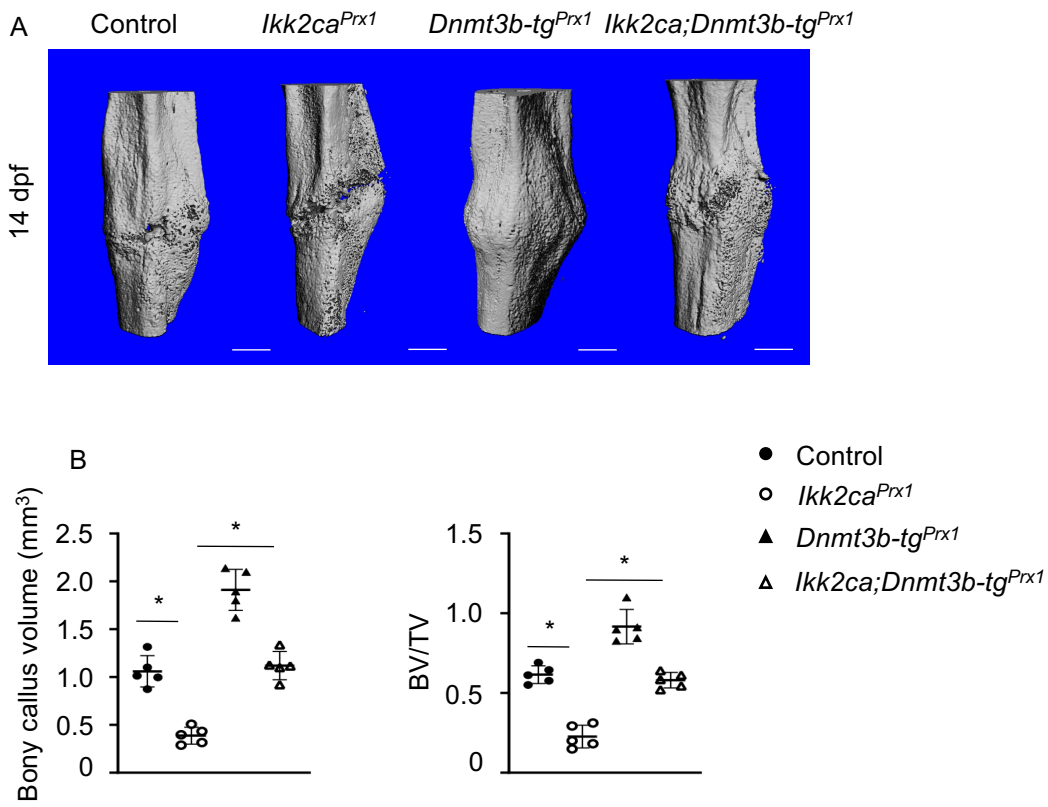


Fig. S19

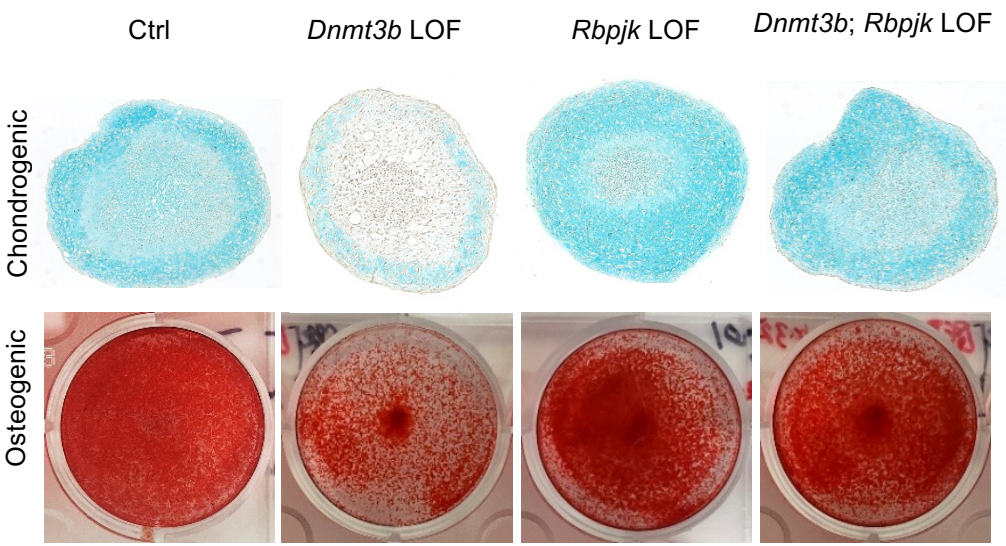


Fig. S20

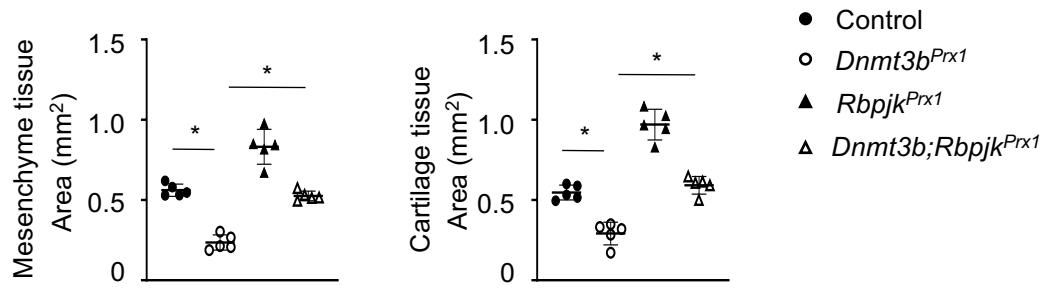


Fig. S21

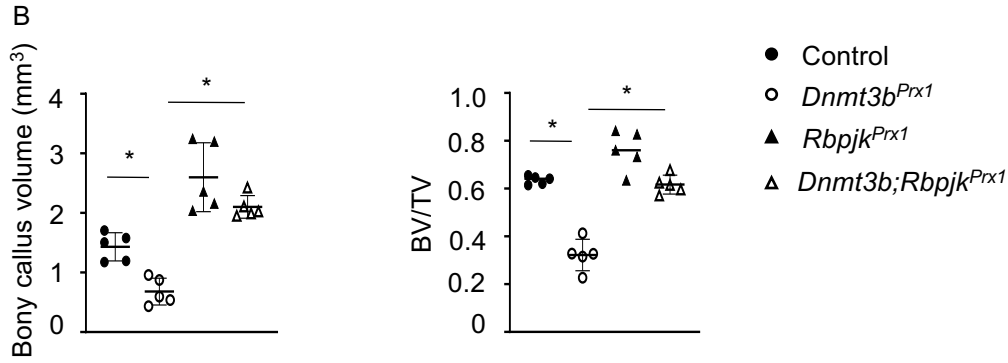
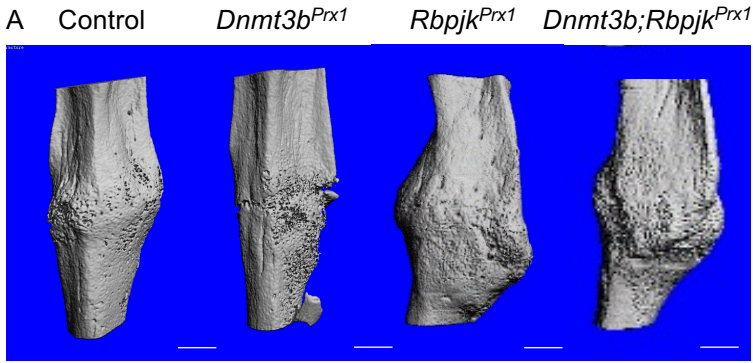


Fig. S22

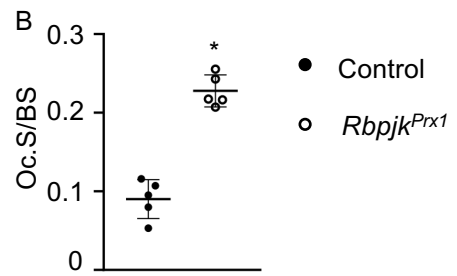
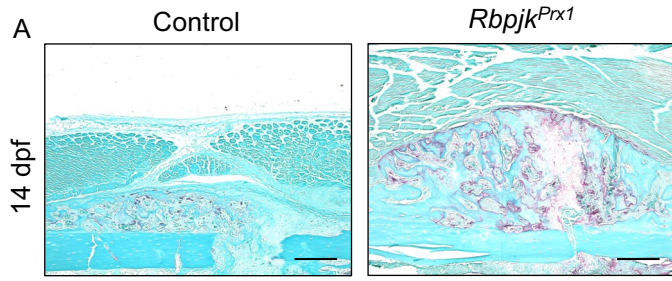


Fig. S23

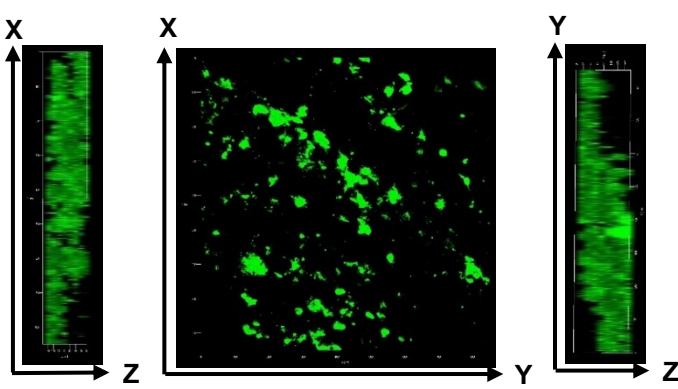
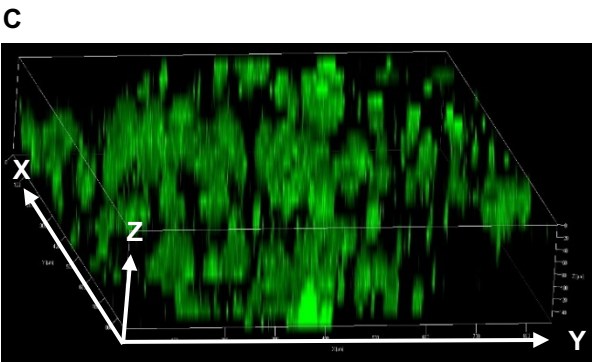
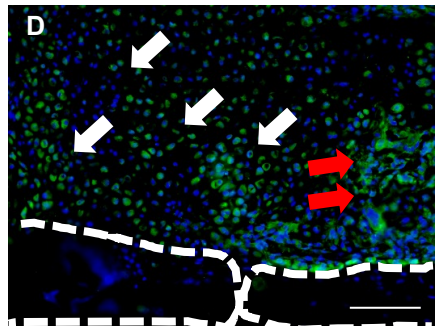
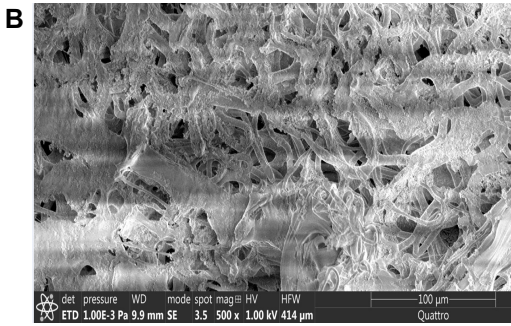
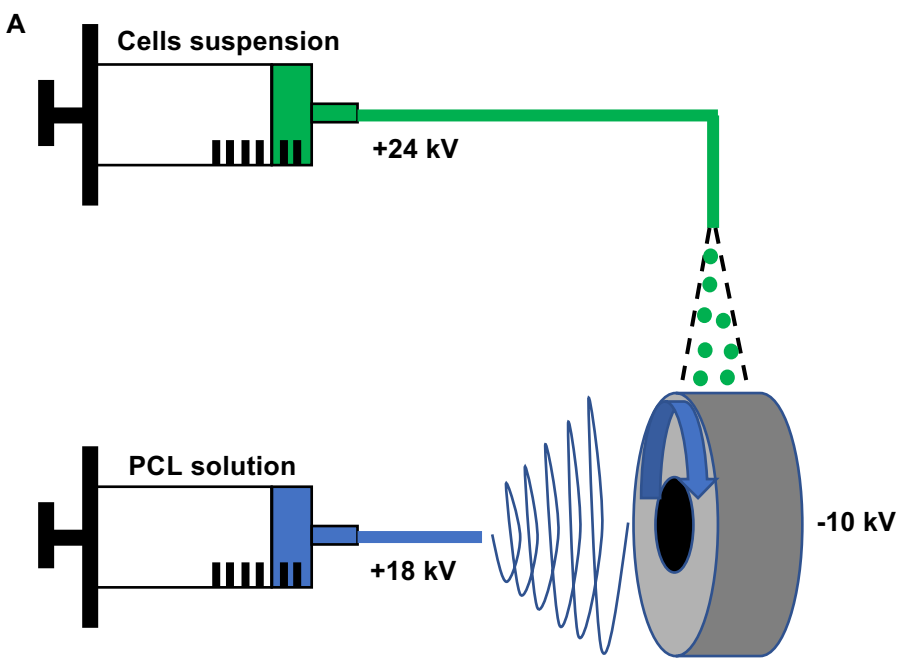


Fig. S24

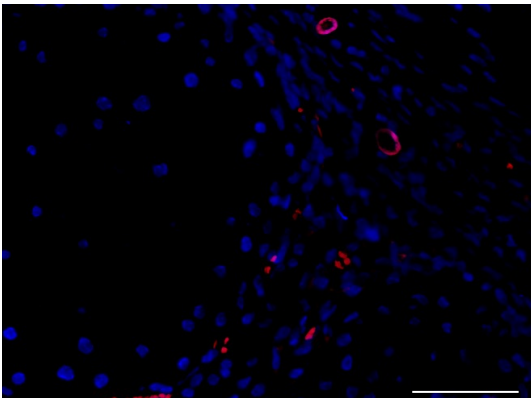
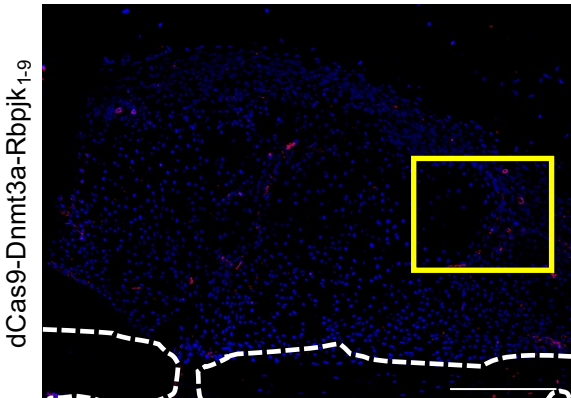
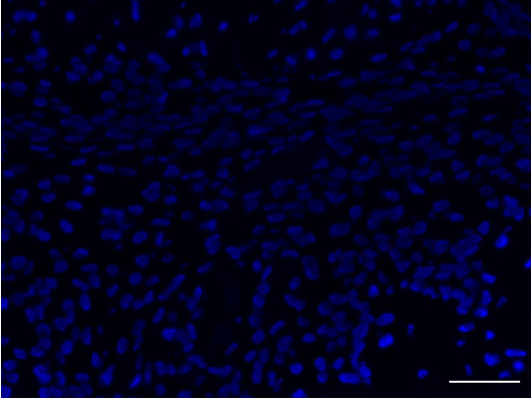


Fig. S25

